applied sciences

MDPI

Article

Impact Simulation of Laser Powder Bed-Fused Polymeric Lattice Structures Using Mooney-Rivlin and Yeoh Hyperelastic Material Models: Calibration and Comparison

Mika Loiselle, William Turnier-Trottier and Vladimir Brailovski *

LAMSI ÉTS, Department of Mechanical Engineering, École de Technologie Supérieure, 1100 R. Notre Dame O, Montreal, QC H3C 1K3, Canada; mika.loiselle.1@ens.etsmtl.ca (M.L.); william.turnier-trottier.1@etsmtl.net (W.T.-T.)
* Correspondence: vladimir.brailovski@etsmtl.ca

Abstract

This study evaluates a methodology for the calibration of the 5-parameters Mooney-Rivlin and Yeoh 3rd-order hyperelastic material models for impact simulations on laser powder bed-fused TPU1301 lattices destined for personal protective equipment. To calibrate the models, bulk normalized specimens were printed and characterized using 400 mm/min uniaxial compression tests. Three 18% density 20-, 30- and 40 mm-thickness lattice structures, namely, Kelvin, body- and face-centered cubic, were manufactured and impact-tested. Using the material models, the impact tests were simulated using LS-Dyna, and their acceleration curves were compared with their experimental equivalents. The simulations accurately depicted the impact behavior of most lattices, but thicker specimens with lower peak accelerations and longer impact durations, such as the 40 mm Kelvin lattice, showed errors reaching 46 and 64% for the Yeoh and Mooney-Rivlin models, respectively. Furthermore, body-centered cubic lattices showed a softer behavior in simulations than experimentally. Overall, the Yeoh model provided the most accurate results across all topologies with an average error of 11.8% compared with 19.6% for Mooney-Rivlin. The methodology used in this study is therefore considered suitable for LPBF-printed TPU1301 lattice structures but would benefit from calibration at higher strain rates, biaxial and shear testing, and better meshing strategies.

Keywords: additive manufacturing; constitutive material model; impact attenuation; strut-based lattice; finite element analysis; TPU

Check for updates

Academic Editor: Dario Croccolo

Received: 9 September 2026
Revised: 1 October 2026
Accepted: 12 October 2026
Published: 14 October 2026

Copyright: © 2026 by the authors. Licensee MDPI, Basel, Switzerland. This article is an open access article distributed under the terms and conditions of the Creative Commons Attribution (CC BY) license.

1. Introduction

Every year, 1.6 to 3.8 million sports or recreational activity-related concussions occur in the United States alone [1]. Although the use of protective equipment such as helmets reduces the risk of such injuries, they are often heavy and uncomfortable, which may negatively impact users' performance or lead to them rejecting the equipment completely [2].

While traditional protective equipment uses closed cell foams produced using conventional expansion and foaming techniques to absorb impacts, additive manufacturing (AM) allows to print complex engineered structures with more precise control over their density and properties. When manufactured from soft polymeric materials, these structures offer a powerful pathway for developing impact-efficient, flexible, lightweight, and tailored protective equipment [3]. Among these polymers, thermoplastic polyurethanes (TPU) hold a large part of the market [4]. TPUs belong to the broader family of elastomers that can

reversibly soften when heated and then harden upon cooling. They exhibit rubber-like elasticity, which enables them to achieve large recoverable deformations under load [5]. This combination of thermoplastic processability and elastomeric performance makes TPUs ideal for architected impact-mitigating structures, especially in applications requiring repeated loading cycles, such as protective gear.

To improve impact attenuation in protective equipment, more recent applications of additive manufacturing and TPUs involve the use of lattice structures. Lattices are three-dimensional cellular architectures typically composed of repeating unit cells. Their repetitive nature allows designers to tailor stiffness and impact attenuation characteristics by adjusting the cell size, geometry and strut/wall thickness [6]. Property gradients can also be incorporated, for example, progressively varying the number and size of cells to gradually stiffen or soften specific zones of a component [7]. These characteristics make lattice structures particularly promising for protective equipment applications [8]. In addition to enabling customized mechanical properties, lattices can also reduce component weight while improving impact attenuation and reducing the acceleration transmitted to the user. According to Chan et al. [9], an appropriately designed lattice structure can provide up to 40% greater impact attenuation than conventional closed cell foam of the same volume. This combination of impact protection and potential wight reduction makes TPU lattice structures an attractive alternative to conventional foams, but only to the extent their geometry and material distribution are optimized to achieve the desired balance between impact attenuation, wearer comfort and lightweight construction.

Few additive manufacturing processes can reliably produce components with complex internal features, such as lattices primarily because such geometries are difficult to fabricate and support during fabrication. Laser powder bed fusion (LPBF) overcomes these limitations by spreading thin layers of polymer powder and selectively fusing each cross-section of a part with a laser. The unfused powder surrounding the part provides inherent support, eliminating the need for dedicated support structures and enabling the fabrication of overhangs, enclosed channels, and architected lattices [10]. After printing, the unfused powder can be removed, and depending on the material and processing conditions, sieved and reused rather than discarded. This reduces the need for dedicated support structures and facilitates the fabrication of highly complex components that would be difficult or impractical to manufacture using other AM technologies [10]. This process is, however, limited to open cell lattices as the unfused powder needs a path to be removed after the printing process.

Nevertheless, researching and developing LPBF lattice structures is costly and time-intensive. A prototypical workflow demands significant upfront investment in machines, materials and labor. The inherent iterative nature of such approach requires producing multiple physical prototypes before convergence to a viable solution. Each iteration carries both financial and environmental costs. In this context, using numerical simulations can reshape the development process by allowing virtual testing of the intermediate design iterations, thus reducing the need for repeated fabrication and allowing to only print the final, optimized versions of the prototypes.

When it comes to the simulation of such complex AM structures, finite element analysis (FEA) provides a powerful framework for evaluating their impact attenuation performance. When dealing with short-duration dynamic events, Sun et al. [11] recommend using solvers based on an explicit solution strategy rather than implicit ones, as explicit methods significantly reduce the computation time while maintaining a good predictability of highly transient problems. However, simulating soft materials with common FEA software packages can be problematic, since most flexible material models available in commercial software such as ANSYS or ABAQUS have been developed for foams and

rubbers and their applicability to AM TPU structure simulations has not been explicitly validated [12].

Furthermore, built-in material models are generally too simplistic to capture the complex behavior of TPUs under dynamic loading conditions, as the response of the models is strongly dependent on both the strain rate and temperature. Very large nonlinear elastic deformations are possible with these polymers, and as a result, they are classified as hyperelastic materials [13]. This feature makes them more complex to model than conventional elastic materials exhibiting much smaller recoverable strains. Therefore, even at a constant temperature, reliable impact simulations of TPU structures require constitutive models capable of representing the nonlinear nature of such hyperelastic and rate-dependent elastomers [14].

Several material models originally developed for other hyperelastic materials, such as foams and rubbers, may also be suitable for AM TPUs. These models use data from standardized tests, including those obtained in uniaxial, biaxial and shear modes, to characterize the behavior of materials under different loading conditions [15]. Once calibrated, they can reproduce the experimentally observed stress-strain response and predict material behavior in different simulated settings. Several hyperelastic constitutive models, including the Ogden, Neo-Hookean and Arruda-Boyce formulations, have been reported in the literature [16]. However, the Mooney–Rivlin and Yeoh models appear particularly promising for representing polyurethane-based materials.

For example, Mohotti et al. [17] successfully simulated impacts on polyurea using a nine-parameter Mooney-Rivlin model calibrated through tensile testing. Similarly, Somarathna et al. [18] replicated this approach with polyurethane and obtained reliable results in uniaxial tension. More recently, Yang et al. [14] reported that a three to five parameters Mooney-Rivlin model is generally sufficient to achieve reliable results without unnecessarily increasing the model complexity and calibration time. The Yeoh model also provides a reliable representation of hyperelastic behavior over a wide range of strain rates [19], making it another potential candidate for AM TPU simulations.

Another advantage of both formulations is their widespread implementation in commercial dynamic simulation software, such as ANSYS LS-DYNA and Abaqus. Their availability in established commercial platforms can facilitate their integration into industrial frameworks, thus making them practical candidates for dynamic simulations of AM TPU components.

It should be mentioned that several studies have investigated the impact response of polymeric lattice structures through numerical simulations [20–22], while others have mainly focused on the methodological aspects of the calibration of hyperelastic material models [13,23]. However, relatively few studies have addressed both aspects within a single framework, and fewer still have sought to develop a methodology suitable for their industrial implementation.

On the one hand, Laird and DuBois [24] combined hyperelastic material model calibration with impact simulations of lattice structures. However, they reported limited agreement between the numerical and experimental results. On the other hand, Diosdado-De La Peña et al. [25] and Shepherd et al. [26] reported more successful outcomes in impact simulations involving hyperelastic lattices. Nevertheless, both studies had specific limitations. Diosdado-De La Peña considered only a single lattice topology and specimen thickness, thereby limiting the assessment of the proposed simulation approach across different lattice geometries. Shepherd et al., meanwhile, investigated lattice structures manufactured via fused filament fabrication (FFF), which involves material and geometric constraints that differ from those associated with laser powder bed fusion (LPBF). There is, therefore, a clear gap in the literature regarding the development and experimental

validation of a robust and industrially applicable framework combining the calibration of hyperelastic material models for impact simulation with their experimental validation across multiple lattice geometries manufactured using LPBF.

Therefore, the objectives of this study are to develop an efficient and reliable methodology for calibrating two hyperelastic material models, namely the Mooney-Rivlin and Yeoh formulations, for the simulation of impacts on lattice structures manufactured using LPBF, and to compare their predictive capabilities. It further intends to determine the most suitable material model for these applications and to investigate how the lattice structure topology and thickness influence the accuracy of numerical predictions. The goal of this approach is to provide a practical methodology for predicting the impact behavior of LPBF-manufactured hyperelastic lattice structures using established commercial simulation platforms.

2. Materials and Methods

The study is divided into two main phases (Figure 1). The first phase, described in detail in Sections 2.2 and 2.4, focused on the calibration of the numerical models used for dynamic simulations. It relied on the quasi-static compression testing of TPU1301 bulk specimens to produce stress-strain curves, which were subsequently used to calibrate the hyperelastic material models for impact simulations of lattice structures manufactured from the same material. The second phase, described in detail in Section 2.3, focused on the dynamic testing of the lattice specimens. The acceleration and impact duration obtained from both simulations and experiments on the lattice specimens were then analyzed and compared to assess the predictive accuracy of the different material models for TPU1301 lattice structures with various topologies and thicknesses.

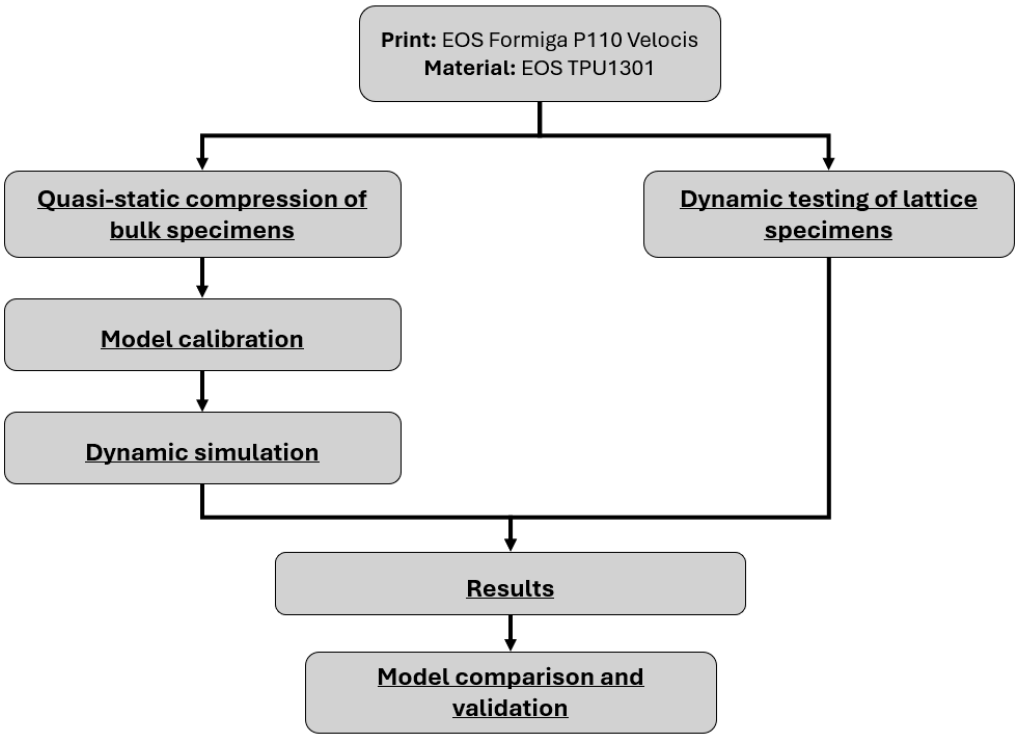


Figure 1. Study workflow.

2.1. Materials and Equipment

The experimental data used in the present work were adapted from a previous study [27], which focused on the characterization of lattice structures manufactured from

TPU1301 powder produced by EOS [28]. TPU1301 is a thermoplastic polyurethane powder made for LPBF. According to the manufacturer, it is the first flexible powder compatible with all EOS printers and can produce parts with a reported Shore A hardness of up to 86, a tensile strength of up to 7 MPa, and an elongation at break of up to 250% (Table 1). EOS recommends TPU1301 for applications in which conventional elastomeric foams are typically used, including footwear, cushioning, and personal protection equipment [28].

Table 1. Printed part properties for EOS TPU1301 polyurethane (taken from EOS GmbH [28]).

Property *	Standard	Unit	Value
Part density	"EOS Method"	g/cm^3	1.11
Hardness	-	Shore A	86
Tensile modulus	ISO 527-1/-2	MPa	60
Tensile strength	ISO 527-1/-2	MPa	XY: 7; Z: 5
Elongation at break	ISO 527-1/-2	%	XY: 250; Z: 90

* Measured at room temperature on parts printed with a 120 µm layer height and unknown exposition setting.

TPU1301 test specimens were printed using an EOS Formiga P110 Velocis system with a 100 µm layer thickness using the "structure_mechanic" parameter set. This exposure parameter set consisted of six contour exposures with alternating hatching recommended for fine structures (feature size < 2 mm) [29]. The remaining of the parameters are not disclosed to the user. The powder used was refreshed with 20% new powder to maintain a bulk density above 0.4 g/cm^3 according to the specifications detailed in Turnier Trottier et al. [27]. The bulk density of the refreshed powder was validated using an ASTM D1895-17 Method R60 flowmeter.

Part positioning was realized with Magics 25.04 software (Materialise NV, Leuven, Belgium). The positioned parts were then sliced into a build volume using the RP-Tools 6.2 add-on (EOS GmbH, Krailling, Germany). The building parameters were prepared using the EOS PSW 3.6 software (EOS GmbH, Krailling, Germany) and then uploaded to the machine for printing. Once printed, the parts were removed from the part cake with compressed air and cleaned using 60–120 grit glass bead blasting to remove excess powder.

2.2. Compression Specimens and Testing Conditions

For this study, two types of test specimen were printed. The first consisted of bulk cylindrical specimens based on ASTM D695 with a diameter of 18 mm and a height of 25.4 mm to avoid buckling (Figure 2a). To reduce the influence of material anisotropy by averaging the directional properties, specimens were printed at a 45° orientation. They were compressed at 70% engineering strain at a strain rate of 0.2625 s^{-1} (400 mm/min) using an MTS Alliance universal testing machine equipped with a 200 kN load cell and flat hardened steel compression platens (Figure 2b) to generate engineering stress-engineering strain curves (Figure 2c). Seven separate specimens were tested to minimize the influence of manufacturing variability on the measured mechanical response.

The selected strain rate of 0.2625 s^{-1} (400 mm/min) corresponds to the maximum testing speed that could be reached by the apparatus without risking damage to the equipment. While this strain rate is considerably lower than what is experienced during impact, the resulting data are used to estimate the average material response at higher strain rates through extrapolation (see also [17]).

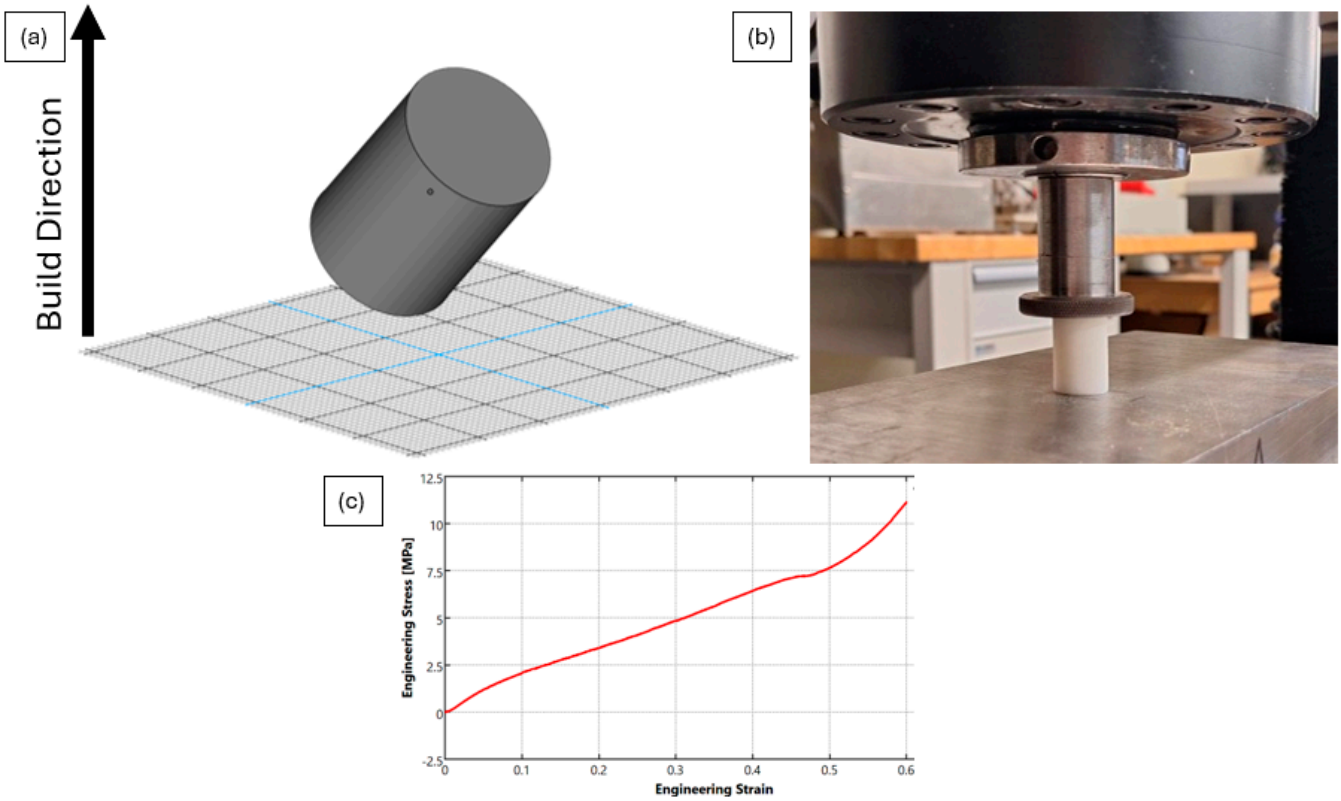


Figure 2. (**a**) Compression test specimen (general view in printing position: oriented by 45° to build plate), (**b**) uniaxial compression testing setup and (**c**) typical stress-strain curve obtained at a 400 mm/min crosshead speed (strain rate 0.2625 s^{-1}).

2.3. Impact Specimens and Testing Conditions

The second type of specimen consisted of Kelvin (KE), body-centered cubic (BC) and face-centered cubic (FC) lattice block structures with overall thicknesses of 20, 30 and 40 mm, as shown in Figure 3a. All lattice configurations had a unit cell size of 10 mm, which was selected during preliminary printing to ensure adequate removal of unfused powder for all lattice topologies. The lattice density was set to 0.2 g/cm^3 (corresponding to a relative material density of 18%) to fall in the middle of the 0.15–0.25 g/cm^3 range identified by Turnier Trottier et al. [27]. This density also ensures that the lattice struts remain within the recommended minimum printable feature size of 1–3 mm [29] while being comparable to the density of competing viscoelastic foams [30].

Two endplates, each 2 mm thick, were added to the lattice specimens to ensure a more uniform load distribution during impact testing. During printing, the lattice specimens were also oriented at 45° relative to the XY plane. In addition to reducing the influence of material anisotropy by averaging the directional properties of the printed parts, this orientation reduced the risk of warping associated with the fusion of large cross-sectional areas, particularly those of the endplates.

Impact tests were conducted on a Cadex monorail impact machine (Cadex Inc, Saint-Jean-Sur-Richelieu, QC, Canada) with a uniaxial accelerometer installed inside a hemispherical impactor. The mass of the carriage assembly was set to 5 kg to approximate the mass of a human head [31]. The impact velocity was set to 4.0 m/s (Figure 3b). This velocity was selected to reproduce the targeted impact conditions while avoiding damage to the testing equipment. The testing temperature was set to 20 ± 2 °C. Only the first impact of each specimen was considered in the analysis to avoid the influence of stress softening [32] on the results. The resulting time-acceleration curves were then processed to extract the peak

linear acceleration (PLA) and the time required to reach this peak from the impact onset, referred to as the "time-to-peak" (TTP), (Figure 3c). Three separate specimens were tested for each lattice topology and overall specimen thickness combination.

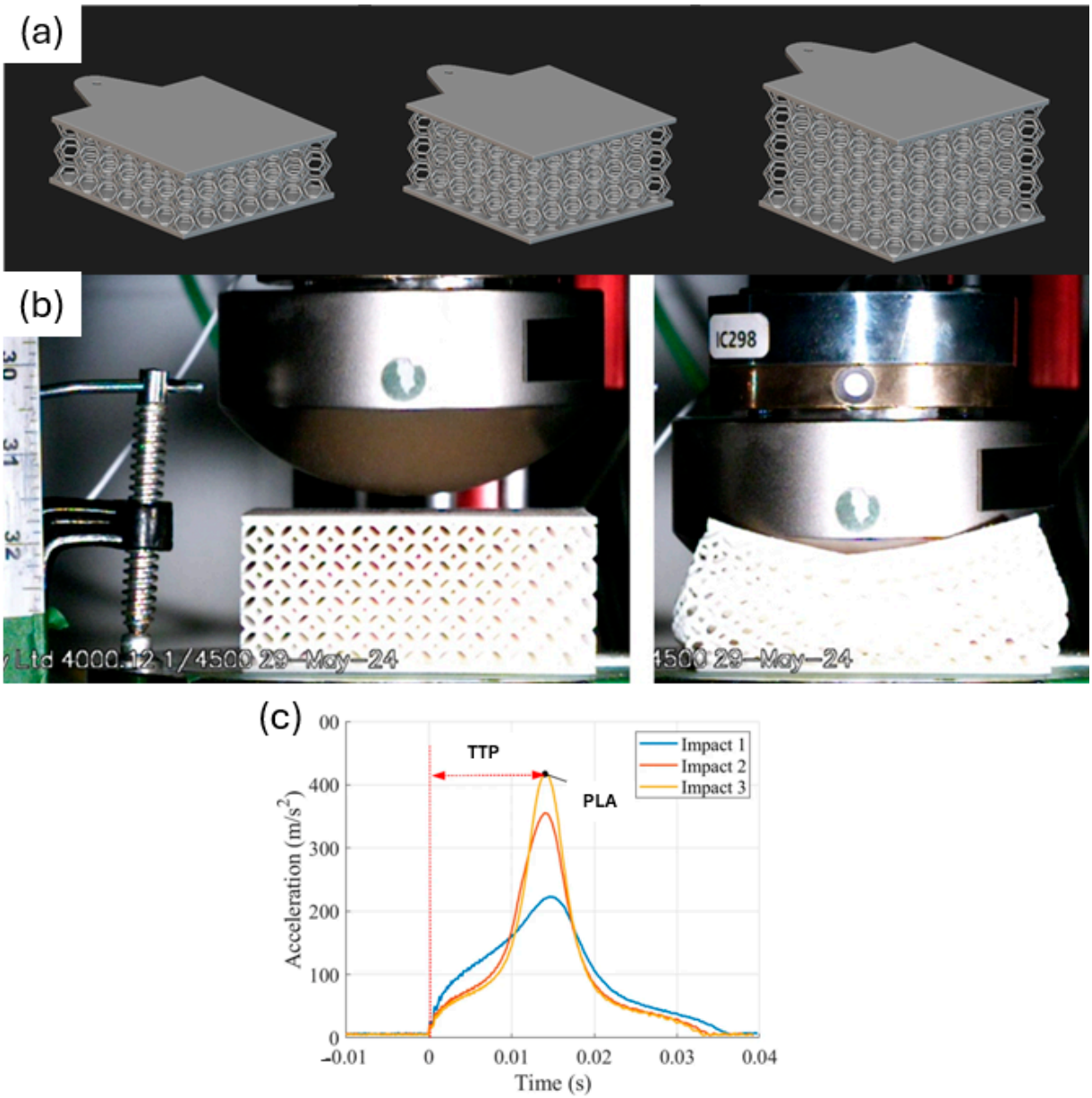


Figure 3. (**a**) Numerical model of a typical dynamic KE specimen and (**b**) structure during dynamic testing; (**c**) typical acceleration diagram (Taken from [27]); only Impact I results were used for analysis.

2.4. Hyperelastic Models

To build a material model capable of simulating a hyperelastic behavior in a dynamic impact setting, seven compression stress-strain curves (Figure 4) obtained with bulk cylindrical specimens were imported into MCalibration 25.1 calibration software (Ansys, Canonsburg, PA, USA). They were then merged into a single curve representing the average behavior of LPBF TPU1301 at a crosshead speed of 400 mm/min (strain rate 0.2625 s^{-1}). The generated average compression stress-strain curve was then curve-fitted with the selected mathematical material model. In the case of this study, the material models used were the 5-parameters Mooney-Rivlin and the 3rd-order Yeoh models.

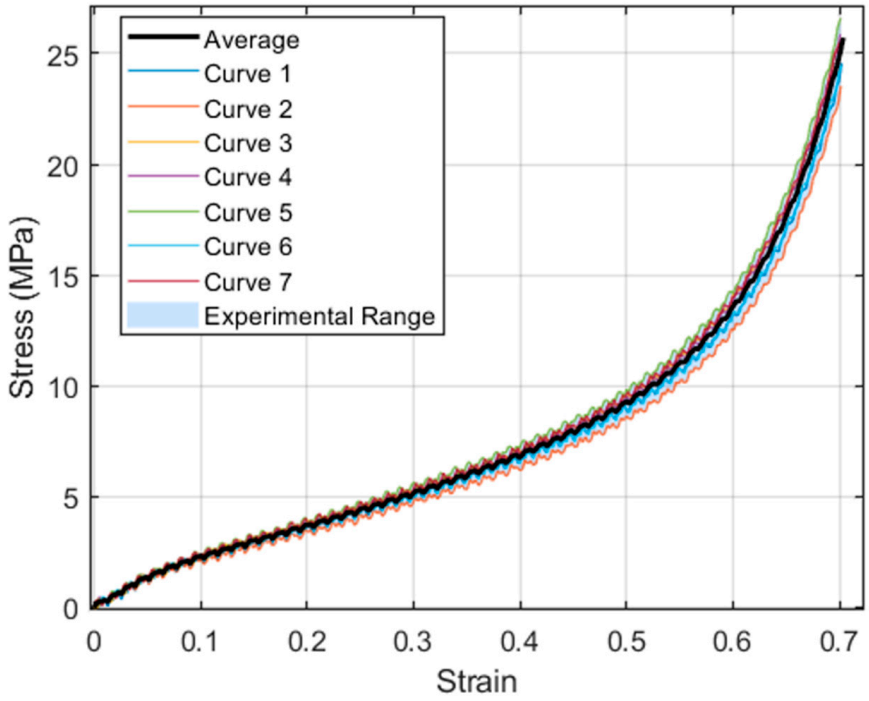


Figure 4. Individual and averaged compression stress-strain curves used for calibration (crosshead speed 400 mm/min; strain rate 0.2625 s^{-1}).

The Mooney-Rivlin model is a hyperelastic material model which is based on the Neo-Hookean model, itself a variation of Hook's law, to represent the non-linear behavior of rubbers and elastomers at medium to large deformations [33]. This model is generally considered suitable for strains of up to 150% [34]. It relies on a strain energy function based on strain invariants I_1 and I_2 calculated from the principal stretches (λ_1, λ_2 and λ_3) and combined with the volume ratio J (J = det (F) where F is the deformation gradient) [23] to create the function's parameters $\overline{I_1}$ and $\overline{I_2}$ in Equation (1) [16]:

$$\begin{cases} \mathrm{I_1} = {\lambda_1}^2 + {\lambda_2}^2 + {\lambda_3}^2 \\ \mathrm{I_2} = (\lambda_1\lambda_2)^2 + (\lambda_2\lambda_3)^2 + (\lambda_1\lambda_3)^2 \\ \overline{\mathrm{I_1}} = \mathrm{J}^{-2/3}\mathrm{I_1} \\ \overline{\mathrm{I_2}} = \mathrm{J}^{-4/3}\mathrm{I_2} \end{cases} \quad (1)$$

The number of parameters can vary depending on the material, but for materials with a stress-strain diagram that exhibits an inflection point, a 5-parameter Mooney-Rivlin model generally provides an adequate representation of the material's behavior [35]. Equation (2) presents the general form of this model [36], including the term for the volume variation energy in the general strain energy function $W = W_{iso} + W_{vol}$ as described by Holzapfel [37] where $W_{vol} = \sum_{k=1}^{q} \frac{1}{D_k}(J-1)^{2k}$. It represents the work of deformation per unit of volume [38].

$$\mathrm{W} = \sum_{\mathrm{i,j=0}}^{\mathrm{N}} \mathrm{C_{ij}}(\bar{\mathrm{I}}_1 - 3)^{\mathrm{i}}(\bar{\mathrm{I}}_2 - 3)^{\mathrm{j}} + \sum_{\mathrm{i=1}}^{\mathrm{N}} \frac{1}{\mathrm{D_i}}(\mathrm{J_{el}} - 1)^{2\mathrm{i}} \quad (2)$$

The number of material constants is a function of the model order. For a 5-parameter Mooney-Rivlin formulation considered in this work, the material parameters are C_{10}, C_{01}, C_{20}, C_{11}, C_{02}. The J_{el} parameter represents the elastic volume ratio and characterizes the volumetric deformation of the material, while D reflects the material compressibility [39]; all parameters determined from experimental data. Since TPU is generally assumed to be

incompressible, the D term in the Mooney-Rivlin model is commonly neglected by setting D = 0. This assumption imposes an elastic volume ratio J_{el} = 1, thereby eliminating the volumetric contribution to the strain energy density while ensuring that the volumetric energy remains finite [39]. This simplification has frequently been adopted in several previous studies [16,26,38].

The Yeoh material model is derived from the Rivlin phenomenological theory of rubber elasticity and differs from the Mooney-Rivlin formulation, primarily in the dependence of the former on the first deviatoric strain invariant, $\overline{I_1}$, rather than on both $\overline{I_1}$, $\overline{I_2}$ [34]. The model was developed to account for the variation of the effective shear response with deformation and is particularly suited to describing the nonlinear behavior of rubber-like materials over a wide range of strains. While the Yeoh model does not explicitly incorporate the second invariant $\overline{I_2}$ like Mooney-Rivlin, it has been shown to accurately describe large deformations in hyperelastic materials while requiring limited experimental data for calibration, particularly data obtained from uniaxial tests. However, its reduced dependence on multiple strain invariants can limit its accuracy when it comes to deformations under multiaxial loading conditions [40].

The strain energy function of the Yeoh model, whose form is similar to that of the Mooney-Rivlin model, is described by Equation (3) [19,34] and contains the same variables as those used in the Mooney-Rivlin formulations. For the 3-parameter Yeoh formulation, they are (C_{10}, C_{20}, C_{30} and D_k).

$$W = \sum_{i=1}^{N} C_{i0}\left(\overline{I_1} - 3\right)^i + \sum_{k=1}^{N} \frac{1}{D_k}(J-1)^{2k} \tag{3}$$

While the commercial ANSYS 2025 R1 Workbench includes both the compressible and incompressible formulations of the Mooney-Rivlin model, it, however, contains only a compressible formulation of the Yeoh model. Given the highly incompressible nature of TPUs, the present study considers the incompressible formulation of the Mooney-Rivlin model and the compressible formulation of the Yeoh model with an almost negligible value of D = 0.001 to avoid treating W_{vol} as infinitely large.

Once the material model was selected, either Mooney-Rivlin or Yeoh, the automatic curve fitting tool was launched to generate the coefficients required for the selected formulation (Table 2). The resulting coefficients were then saved and imported directly into the corresponding material model section of the ANSYS engineering data module.

Table 2. Material models' calibrated coefficients (note that coefficients C and D of the Mooney-Rivlin and Yeon models are taken as they are marked in the ANSYS software and should not be interchanged).

Mooney-Rivlin (MPa)		Yeoh (MPa)	
C_{10}	−24.011	C_{10}	4.0608
C_{01}	29.424	C_{20}	−1.8532
C_{20}	103.751	C_{30}	2.4232
C_{11}	−285.001	D_1	0.001
C_{02}	211.332	D_2	0.001
D_{1-5}	0	D_3	0.001

2.5. LS-Dyna

After the custom material models were imported into ANSYS 2025 R1 Workbench, the simulation setup was built to replicate the experimental testing conditions and solved using the LS-Dyna 14.1 solver. The computer-aided design (CAD) model was prepared in Creo Parametric 12.4 (Parametric Technology Corporation, Boston, MA, USA) with two separate

bodies: a model of the impactor and the tested structure. The boundary conditions were defined by fixing the base of the lattice block, consistent with the experimental setup in which the specimens were glued to the anvil during the impact tests. Frictional contact was also defined between the impactor and the lattice block, with static and dynamic friction coefficients of 0.7 and 0.6, respectively, based on the experimental results of Yahiaoui et al. [41]. To assess the validity of these assumptions, a 30 mm-thickness BC lattice structure was simulated using both conditions, i.e., frictionless and frictional contacts. The use of frictional contact resulted in peak acceleration values approximately 5% closer to the corresponding experimental measurements, thereby supporting the use of frictional contact conditions in the numerical model. To simulate the monorail testing machine, a rigid body constraint limiting the impactor's degrees of freedom to vertical translation only was also added.

Additionally, an asymmetric manual contact region was defined, with the impactor face designated as the target region and the top end plate of the specimen designated as the contact region due to its comparatively lower stiffness [42]. To replicate the experimental tests, the impactor was assigned a mass of 5.0 kg and an initial velocity of 4.0 m/s, while a gravitational acceleration of 9.81 m/s^2 was applied in the simulations (Figure 5).

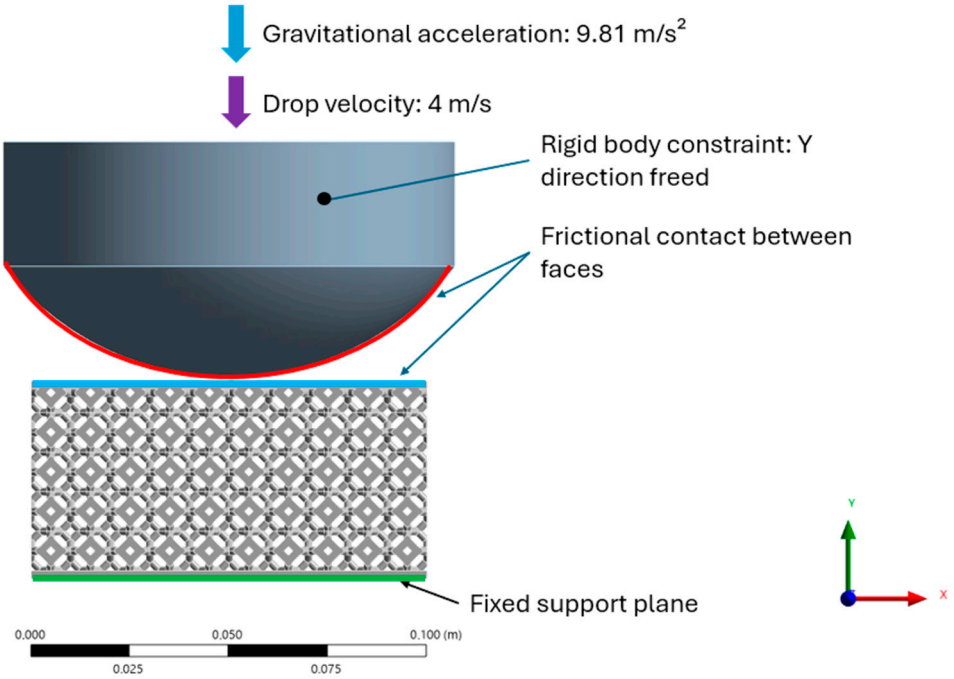


Figure 5. ANSYS 2025 R1 Workbench model parameters for LS-Dyna simulation.

A Tet4 tetrahedron mesh was then applied to the lattice structures to accurately represent their complex geometry. Tetrahedral elements are well suited to geometries with complex and curved surfaces [43] and often provide shorter solution times compared to more demanding mesh configurations [44]. After a convergence study on a 30 mm BC lattice with element sizes ranging from 1.5 mm to 0.75 mm, an intermediate element size of 1 mm was selected. This choice was based on the observation that the PLA and TTP results obtained with the 0.75 mm element size deviated by only 5% from those obtained with the 0.5 mm element size, while requiring more than 38.5 h of additional computational time. Therefore, the 1 mm element size was considered to provide an appropriate balance between spatial resolution and computational efficiency, while ensuring a minimum of two elements across the width of each lattice strut.

Based on the duration of the experimental impact tests, the simulation end time was set to 0.02 s. The output time interval was maintained at the default value of 0.001 s. The simulated directional acceleration in the Y-direction (expressed in m/s^2) was converted to units of impact acceleration (G) by dividing the calculated acceleration values by 9.81 m/s^2. This conversion allowed the simulated acceleration-time curves to be directly overlaid with their experimental equivalents for comparison.

3. Results

3.1. Dynamic Compression Testing

Using data from three separate impact tests for all the lattice types and thicknesses, the corresponding acceleration-time curves can be traced. Figure 6 presents an example of three impact tests on 30 mm-thickness Kelvin lattice specimens. Each set of three experimental curves can then be averaged for comparison with the corresponding simulated equivalents.

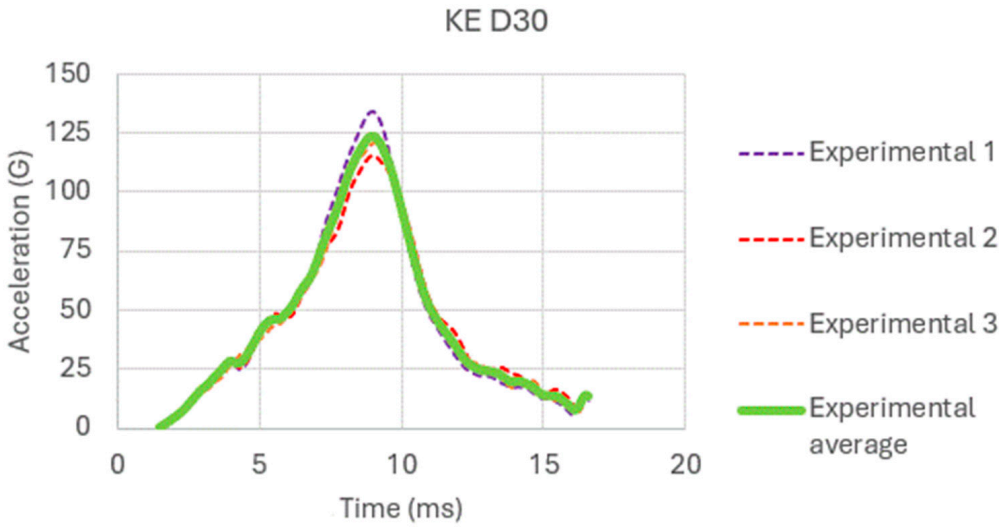


Figure 6. Experimental acceleration curves for impact tests on 30 mm-thickness Kelvin (KE) lattice structures.

Using the impact averages, the effects of reducing the overall thickness of the lattice specimens with different topologies (KE, FC and BC) become clear. As demonstrated by the KE lattices (Figure 7a), thicker specimens result in lower-impact accelerations and longer time-to-peak values, as these structures dissipate energy better and spread the collision over longer periods of time. FC and BC structures show an even greater difference between thicknesses (Figure 7b), especially for the lower thickness of 20 mm, where the peak acceleration surpasses 250 G. However, only the BC structures (Figure 7c) exhibit very similar behaviors, both in terms of PLA and TTP for 30 mm and 40 mm specimens.

Overall, a comparison of the three structure types indicates that the KE lattice is more efficient at absorbing kinetic energy than the other two structures, particularly for thinner specimens. While the FC structures exhibit relatively consistent impact attenuation performance across the investigated thicknesses, the BC structures exhibit substantially lower performances for the thinnest specimens. Although each lattice type exhibits a distinct behavior in terms of peak acceleration, the tendency for thicker specimens to take a longer time to reach the peak remains. This behavior is consistent with the expected increase in deformation capacity and energy dissipation associated with a greater specimen thickness.

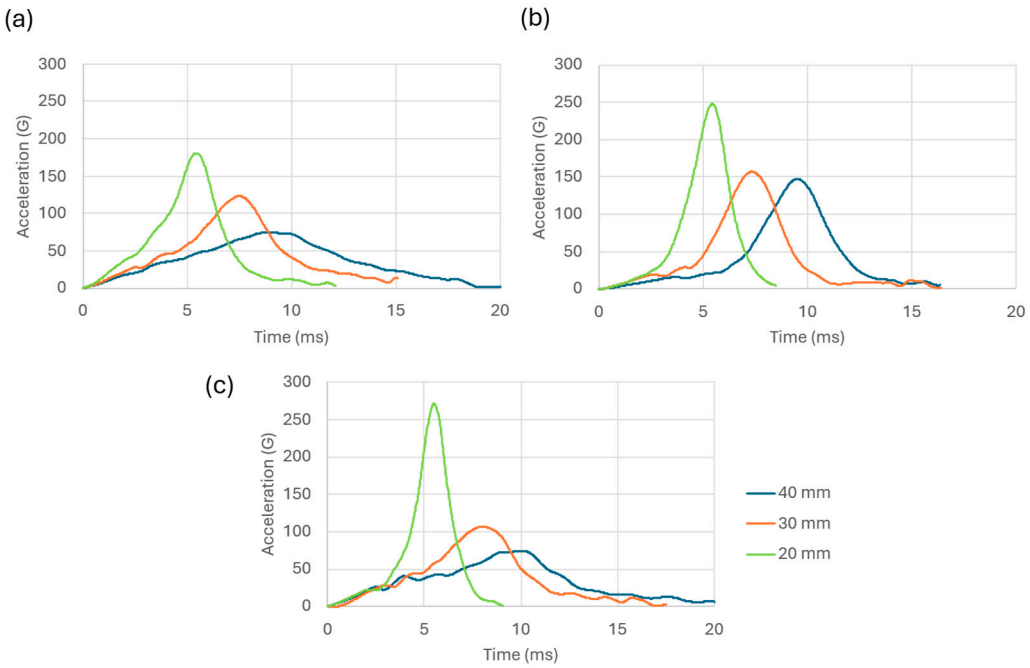


Figure 7. Average acceleration-time curves for different lattice types and thicknesses: KE (**a**), FC (**b**) and BC (**c**).

3.2. Dynamic Compression Simulations

After importing the Mooney-Rivlin and Yeoh material models' parameters in ANSYS as custom materials, the experimental impact tests were reproduced using LS-Dyna. The results for each thickness with all three types of lattices obtained using both material model formulations are presented in Figure 8.

In most cases, the simulated lattices seem to show the same tendency of decreasing the peak acceleration with increasing specimen thickness for both Yeoh and Mooney-Rivlin results, with a smaller difference between the 30 and 40 mm specimens than between the 30 and 20 mm ones. Of particular interest is the fact that the 30 and 20 mm KE specimens show almost indistinguishable acceleration behaviors for both material models (Figure 8a,b).

A significant difference can be observed between the results obtained using the Yeoh and Mooney-Rivlin models. Overall, the Yeoh model predicts more pronounced differences between the 30 and 40 mm thick specimens (Figure 8a,c,e), whereas such differences are considerably less pronounced when using the Mooney-Rivlin model (Figure 8b,d,f).

Furthermore, using the Yeoh model, the FC lattices appear to provide the lowest impact attenuation performance at low thicknesses, but the highest performance at higher thicknesses, when compared with other structures. This results in lower PLAs and longer impact durations in Figure 8c, although they are very close to those of the BC structures in Figure 8e.

In the case of the Mooney-Rivlin model, the PLAs and the TTPs are substantially different from those observed with the Yeoh model, but the same observation can be made. Without changing the trend in the structures' performance, the models appear to present different behaviors for the same simulated material. The FC structures' simulated acceleration curves (Figure 8c,d) in particular appear to be very similar to the BC structure results (Figure 8e,f) for the Yeoh model, but differ by larger margins for the 40 mm specimen when compared with the Mooney-Rivlin results. The BC and the FC structures also appear to have larger discrepancies between Mooney-Rivlin and Yeoh results than what can be observed with the KE acceleration curves.

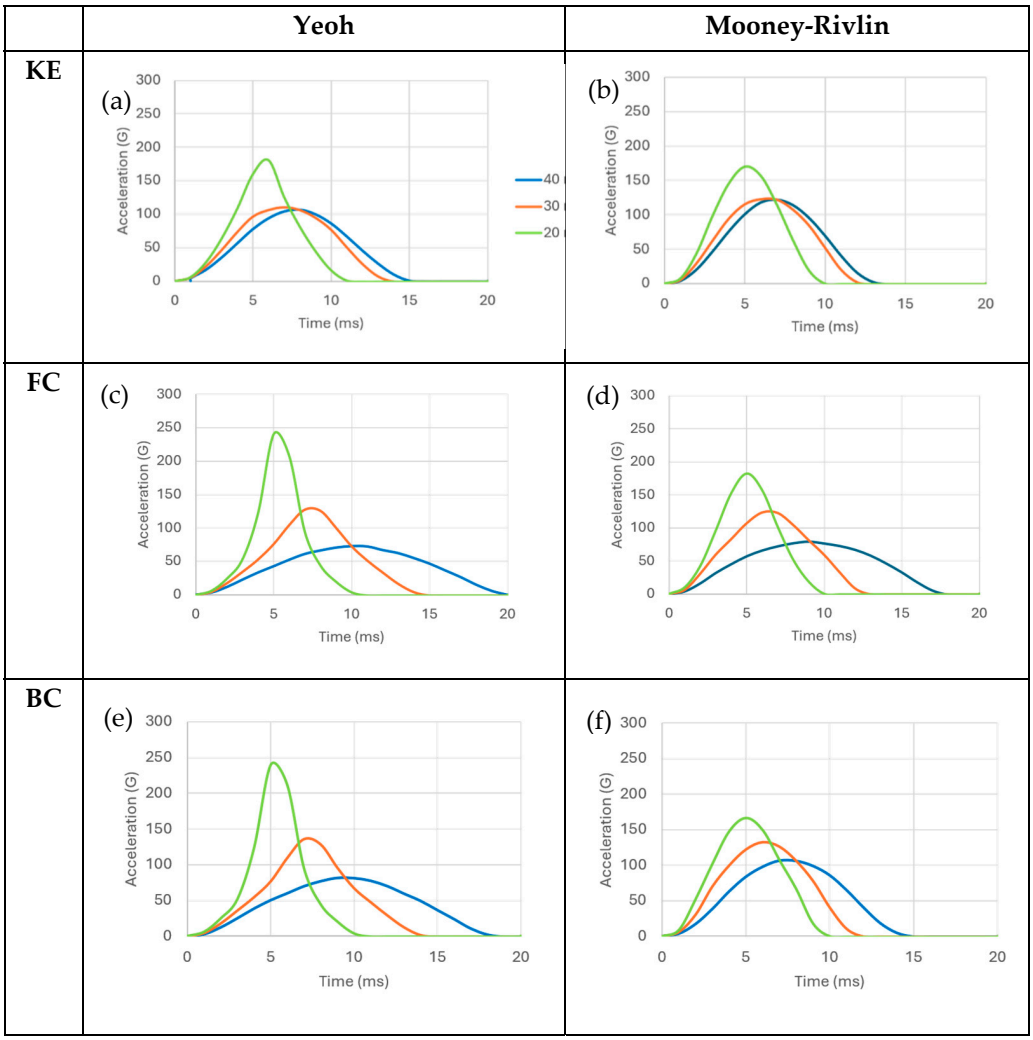


Figure 8. Acceleration curves from the impact simulations of three thicknesses of KE (**a**,**b**), FC (**c**,**d**) and BC (**e**,**f**) lattices for both Yeoh (**a**,**c**,**e**) and Mooney-Rivlin (**b**,**d**,**f**) models.

3.3. Comparison: Simulation vs. Experiment

From the KE lattice acceleration curves shown in Figure 9, both material models provide a close approximation of the experimental behavior of the thinner specimens, both in terms of peak acceleration and impact duration. However, larger discrepancies are observed for the thicker specimens. The simulations exhibit a considerably rounder profile than the experimental curves, thus being different from the gradual increases in acceleration observed experimentally, which is associated with the progressive attenuation of the impactor's descent without bottoming out.

In the case of the FC lattices, the simulated curves follow the same trends as the experimental curves in terms of impact duration but are less accurate in predicting peak accelerations for the thinner specimens, as shown in Figure 10b,c. For the 40 mm-thickness specimens shown in Figure 10d, the simulations exhibit a behavior similar to that observed for the KE D20 specimen in Figure 9b, with peak acceleration and impact duration values nearly identical to their experimental equivalents. Overall, both models appear to provide more accurate predictions for thicker FC lattices and thinner KE lattices, while showing lower accuracy for thinner FC lattices and thicker KE lattices.

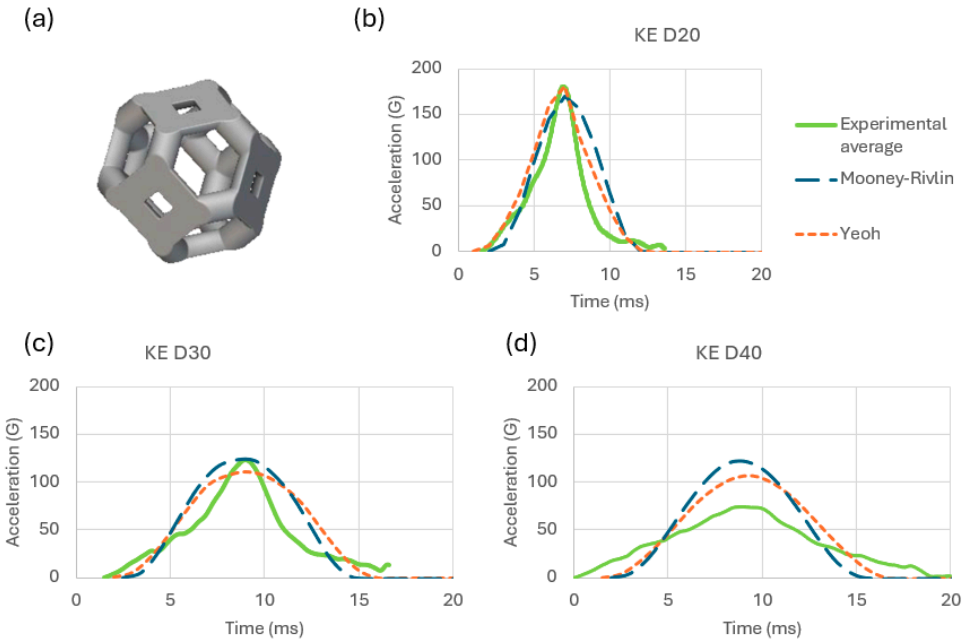


Figure 9. KE lattice cell (**a**) and corresponding experimental and numerical impact acceleration curves for 20 (**b**), 30 (**c**) and 40 mm-thickness (**d**) specimens.

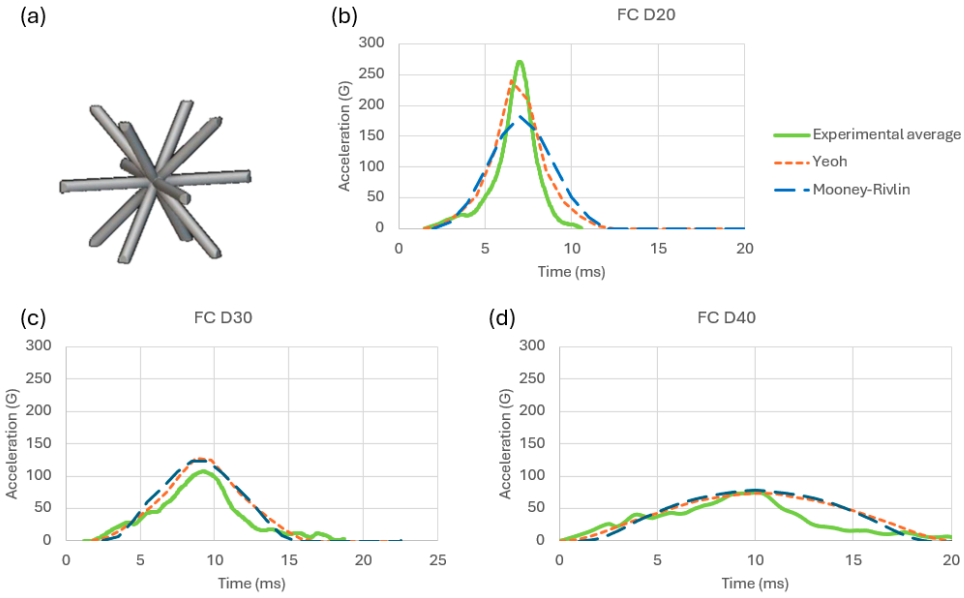


Figure 10. FC lattice cell (**a**) and corresponding impact acceleration curves for 20 (**b**), 30 (**c**) and 40 mm thick (**d**) specimens.

For the BC lattice simulations, the results presented in Figure 11 differ substantially from their experimental counterparts in all the instances, distinguishing them from their FC and KE counterparts, for which the simulation more closely follows the experimental results. The substantially lower peak accelerations and gentler curvatures suggest that the simulations may underestimate the effective stiffness of the BC lattice structures. This discrepancy indicates that the material models used may not adequately capture the deformation mechanisms associated with the BC topology. Despite the relatively poor agreement observed in terms of peak accelerations, the simulated time-to-peak values follow the same trend as the experimental results, indicating that the simulations are able to capture the general temporal response of the BC structures. In this regard, the Mooney-

Rivlin model exhibits more accurate results, while the Yeoh model is more accurate in terms of PLAs, with the exception of the 40 mm specimen.

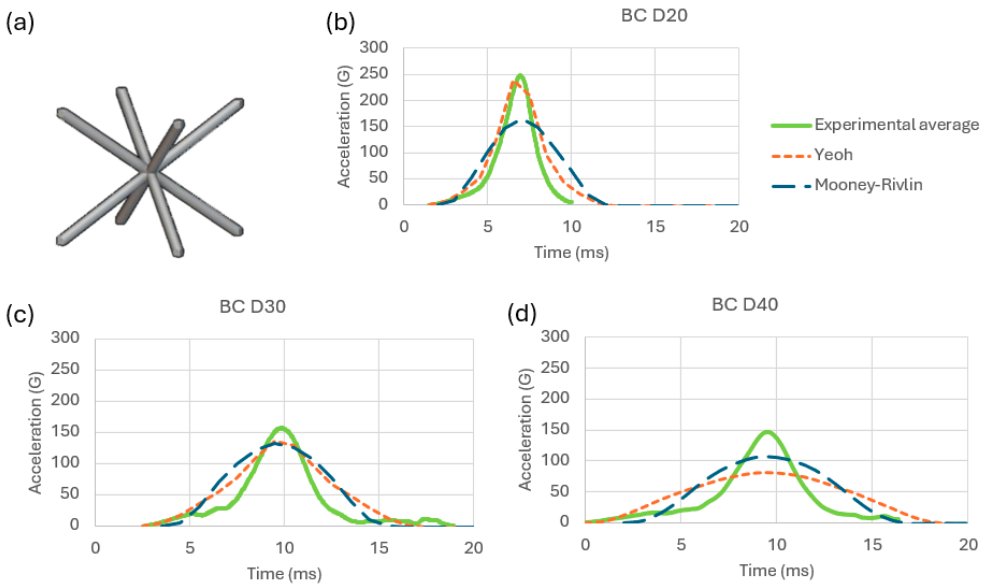


Figure 11. BC lattice cell (**a**) and corresponding impact acceleration curves for 20 (**b**), 30 (**c**) and 40 mm thick (**d**) specimens.

4. Discussion

While the simulation results obtained from both models show relatively good concordance with experimental results overall, discrepancies remain under certain circumstances. To better appreciate these discrepancies, the PLAs and TTPs from both models and their experimental averages were gathered in Figure 12 and compared by lattice thicknesses. The variability in the experimental results from the three impact tests conducted for each lattice type and thickness is represented by error bars. The detailed values of these PLAs and TTPs can be found in Appendix A (Tables A1–A3) along with those of the experimental results.

When comparing these results, the simulated thinner specimens appear to systematically produce lower accelerations than their experimental counterparts for the KE, FC and BC lattices (Figure 12a,c,e). Furthermore, in their current implementation, both models appear to mostly underestimate the behavior of the BC lattices.

The analysis of PLA and TTP across all the specimen thicknesses and lattice topologies in Figure 12 highlights both the conditions under which the models work better and those in which they have difficulties in capturing experimental impact behavior.

Overall, there seems to be good agreement between the simulated and experimental TTP values. In some cases, particularly for the Yeoh model, differences in TTPs could be attributed to the temporal resolution used in the simulations. This hypothesis was verified by performing an output interval sensitivity study conducted using the Yeoh model on a 30 mm-thickness BC lattice structure. This study showed that reducing the output interval from 0.001 to 0.0005 s decreased the initial TTP error of 0.4 ms (7.3%) down to 0.1 ms (2%). Further reducing the output interval to 0.0002 s reduced the TTP error to 0.007 ms (0.1%) for this particular specimen. These results suggest that the output time interval may have a non-negligible effect on the accuracy of TTP calculations. However, the discrepancies between the simulated and experimental TTP values are comparable to the observed specimen-to-specimen variability, with an average scatter of $\pm$0.17 ms in the experimental TTP data (Table A2). A more intensive investigation of the effect of output time interval was considered beyond the scope of the present study and left for further refinement in the next phase of the project.

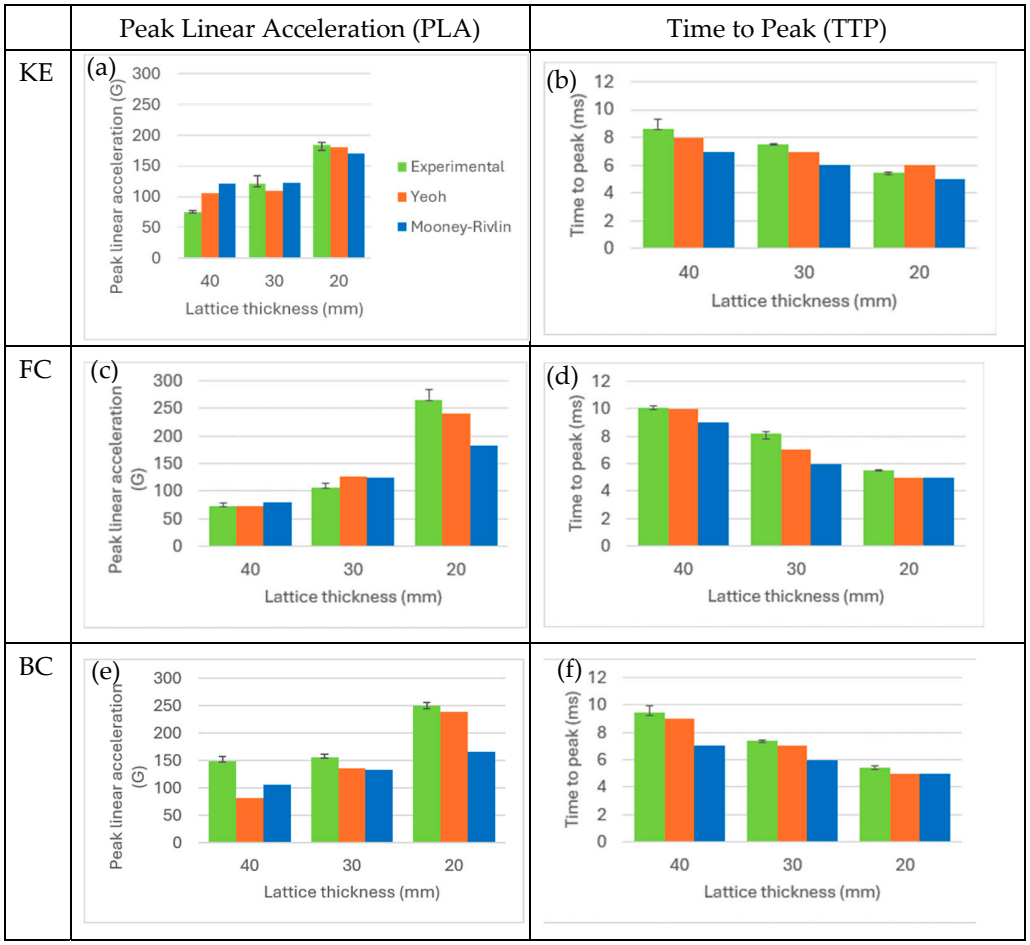


Figure 12. Comparisons of the experimental (averaged) and simulated (Mooney-Rivlin and Yeoh models) PLA and TTP values obtained for KE, FC and BC structures of variable thicknesses. PLA for KE lattice (**a**), TTP for KE lattice (**b**), PLA for FC lattice (**c**), TTP for FC lattice (**d**), PLA for BC lattice (**e**), TTP for BC lattice (**f**).

The PLA values, however, do not display the same small and systematic discrepancies. While most simulated results for the KE and FC specimens are relatively close to the experimental values, the BC specimens in Figure 12e,f show substantially larger discrepancies for both material models, with differences reaching up to 45%. This suggests that the deformation mechanisms governing the impact response of the BC topology may differ from those captured by the two models tested. In addition, the largest discrepancies between experimental and simulated PLA results are observed for the thicker KE and BC structures. For the KE lattices, the simulations overestimate the PLA by about 43% with the Yeoh model and by 64% with the Mooney-Rivlin model in Figure 12a. Conversely, for the BC lattices, the PLA is underestimated by 45% with the Yeoh model and by 29% with the Mooney-Rivlin in Figure 12e. The only 40 mm-thickness specimens that exhibited close agreement with the experimental results are the FC lattices in Figure 12c. The corresponding PLA errors were only 0.1% for the Yeoh model and 8.2% for the Mooney-Rivlin.

The discrepancies identified above may indicate limitations in the calibration of the material model when applied to the higher deformation rates associated with the investigated impact conditions. The current calibration method is orders of magnitude slower than a real impact, which implies a large extrapolation of the non-linear behavior of the material, perhaps leading to a large part of the inaccuracies in the results obtained. Therefore, in its current state, the methodology presented in this study should be considered primarily for

pre-screening lattice types during PPE design, rather than an accurate representation of their real-world performance.

Ideally, to address inaccuracies arising from calibration at lower strain rates, the material models should be calibrated using experimental data obtained at strain rates as close as possible to those encountered during the targeted impact. Such tests could be conducted using a more specialized apparatus, namely, a Split Hopkinson Pressure Bar as suggested by Yang et al. [14]. Additional tests such as biaxial and shear tests could also be performed to explore their effect on accuracy, as pointed out by Keerthiwansa et al. [45]. However, access to this equipment is limited, and conventional testing methods, such as that used in the present study, often represent the only practical option. Alternatively, the same lattice structures could be simulated using models requiring only tensile data, such as the Ogden model, which has shown promising results on Kelvin lattices [25].

The larger discrepancy between the experimental and simulated behavior of the BC lattices under impact, observed in both the acceleration curves and the PLA/TTP graphs, may be attributed to the longer unbraced struts present in the lattice geometry. In the simulations, these struts tend to buckle under the impact load. However, if, under experimental conditions, the struts bend before reaching the buckling regime, this could result in a stiffer experimental response and, consequently, higher measured acceleration than predicted by the simulations. This explanation remains hypothetical, since the images obtained during the impact tests were not sufficiently clear to accurately assess the actual deformation mode of the struts.

Furthermore, using perfect CAD models in the simulation, rather than 3D representations of the samples incorporating real process-induced imperfections, may also contribute to the differences in deformation modes between simulations and experiments. The selected mesh size may have further contributed to the discrepancies between the experimental and simulated results. In the simulations, a mesh size of 1 mm was selected based on a convergence study conducted on a 30 mm-thickness BC lattice. This study considered mesh sizes ranging from 1.5 to 0.75 mm and showed that reducing the mesh size from 1.5 to 0.75 mm, and consequently, increasing the computational time from 1.5 to 40 h, resulted in less than a 5% difference in PLAs. This difference in accuracy was considered insufficient to justify the substantially increased computational cost, particularly given the comparative nature of this study. However, the 1 mm mesh may have been too coarse to accurately capture the deformation behavior of the longer struts of the BC lattice.

Further investigation using alternative meshing strategies or beam elements could, therefore, improve the representation of the struts' deformation while limiting additional computational cost. Beam elements were initially disregarded because they do not consider cross-section deformations that could affect the simulated specimen's behavior, but it would allow for a much lower node count in each simulation, would provide faster solve times and could allow for more predictable deformations in struts. In the context of an initial screening for new potential lattice types for helmets, the discrepancies in cross-sections could be small enough to justify the tradeoff in simulation accuracy.

Once a suitable meshing strategy is established across the different lattice thicknesses and geometries investigated in the present study, its performance should also be evaluated using other hyperelastic polymers. That would determine whether the methodology is sufficiently robust and repeatable for broader applications regarding the research and development of lattice-based protective equipment. Finally, comparing the collapse behavior of the BC lattice under impact with its simulated counterpart using a flat impactor would provide an additional means of validating the predicted deformation mode of the struts. Such testing could help determine whether the observed bending-buckling behavior is responsible for the discrepancy between the experimental and numerical results.

Overall, although the constitutive models exhibited limitations when used to simulate the impact behavior after calibration at a low strain rate, the results remain encouraging. The comparison between the Yeoh and Mooney-Rivlin models suggests that the Yeoh model is better suited to representing the impact response of LPBF 3D printed lattices across the geometries investigated in the present study when both are calibrated using conventional material testing machines and uniaxial compression data alone. Its predictions were consistently closer to the experimental results than those of the Mooney-Rivlin model, both in terms of PLA and TTP, with difference being particularly striking for thinner specimens. These thinner configurations are also more representative of the dimensions used in protective equipment, such as helmets [46]. It is still important to note that this comparison might yield different results if the calibration is done at the same strain rate as the experimental impact, so these conclusions are strictly based on the results from a low-strain-rate calibration.

The TTP values predicted using the Yeoh model were systematically closer to, or comparable with, the experimental values relative to the Mooney-Rivlin model, with a difference of about 13% (1 ms) instead of the near 20% error of the latter. Its PLA predictions were also mostly in closer agreement with the experimental results, as previously mentioned, with an overall average error of 11.8% compared to around 19.6% with Mooney-Rivlin across all topologies. This improved performance may be attributable to the large deformations experienced during impact, for which the Mooney-Rivlin model can be less suitable when calibrated from axial data alone. The model tends to provide more accurate predictions at lower strains, as demonstrated by Emminger et al. [47], and accurately capturing more complex deformation behaviors with it may require calibration data from multiple loading modes.

Further investigation of alternative constitutive models would therefore be valuable, particularly of models that can be calibrated using uniaxial data while accounting for phenomena such as stress softening. Such models could potentially provide improved predictions for different lattice geometries subjected to repeated compression and impacts. Additionally, while three different lattice types have been tested in an attempt to validate a model suitable for any strut-based lattice, other lattice types, such as triply periodic minimal surface (TPMS) and bio-inspired lattices, should be tested using the same calibration steps to validate if it can be used as a universal screening method for lattices. Since the constitutive models are calibrated to simulate the material's behavior itself, the results should be similar to those of this study, but the large discrepancies in the BC lattice results suggest there may be a need for adjustments in the methodology for other lattice types that would need to be identified before any serious application. These approaches are beyond the scope of the present study, but represent a promising direction for developing a more general and accurate constitutive modeling methodology for LPBF-printed TPU lattices.

5. Conclusions

This study investigated the feasibility of using uniaxial compression tests at relatively low strain rates only to calibrate the Mooney-Rivlin and Yeoh hyperelastic material models and evaluated their ability to predict the dynamic impact behavior of LPBF printed TPU1301 lattices intended for personal protective equipment. Compression tests were performed to calibrate both models, while impact tests were conducted on lattice specimens with a relative density of 18%, three different topologies (KE, BC and FC), and three different overall thicknesses (20, 30 and 40 mm). The calibrated models were subsequently implemented in LS-Dyna to simulate the impact tests, and the numerical results were compared with the corresponding experimental data.

Overall, the simulations were effective at capturing the impact response of the lattices with reasonable accuracy. However, this accuracy decreased in the 40 mm KE specimen and significant deviations were observed in the BC results when compared to the experimental data. These discrepancies suggest that the calibration methodology requires further refinement and should only be used, in its current state, as a method to pre-screen lattices before designing PPE. Potential sources of error include the use of calibration data obtained at strain rates that are not representative of the targeted impact conditions, the limited range of loading modes used for the calibration, and the selected meshing strategy.

When comparing the constitutive models, the Yeoh model consistently provided results in closer agreement with the experimental tests than those from Mooney-Rivlin across most geometries and thicknesses when calibrated using uniaxial compression data exclusively. This could indicate that the Yeoh model is better suited for simulating a range of TPU1301 lattice-based LPBF-manufactured PPE designs in a virtual development environment when the testing data or more advanced calibration equipment are in limited supply.

Future research should assess the source of the discrepancy found in the KE 40 mm specimen results and test different calibration strain rates to improve the general accuracy of the results. Exploring different meshing strategies to accelerate simulations and refining lattice strut representations along with additional calibration loading modes, such as simple shear, volumetric compression and biaxial tension, could also prove instrumental in the development of a more robust methodology adapted for virtual prototyping of LPBF-printed TPU lattice structures for PPE applications.

Author Contributions: Conceptualization, M.L., W.T.-T. and V.B.; Project administration, V.B.; Methodology, M.L.; Formal analysis, M.L.; Investigation, M.L., W.T.-T. and V.B.; Writing—original draft preparation, M.L. and W.T.-T.; Writing—review and editing, M.L., W.T.-T. and V.B.; Visualization, M.L.; Supervision, V.B.; Funding acquisition, M.L. and V.B. All authors have read and agreed to the published version of the manuscript.

Funding: This research was funded by a grant from the Natural Sciences and Engineering Research Council of Canada (NSERC Grant number: 618618) | CRSNG RGPIN-2020-05800.

Institutional Review Board Statement: Not applicable.

Informed Consent Statement: Not applicable.

Data Availability Statement: The raw data treated in this study are included in the Appendix A. Further inquiries can be directed to the corresponding author.

Conflicts of Interest: The authors declare no conflict of interest.

Abbreviations

The following abbreviations are used in this manuscript:

AM	Additive manufacturing
LPBF	Laser Powder Bed Fusion
TPU	Thermoplastic Polyurethane
FEA	Finite Element Analysis
FFF	Fused Filament Fabrication
KE	Kelvin
BC	Body-Centered Cubic
FC	Face-Centered Cubic
PLA	Peak Linear Acceleration
TTP	Time-To-Peak

Appendix A

Appendix A.1. PLA and TTP Impact Data Results per Thickness for KE Lattice

Table A1. KE lattice experimental and simulated impact results per thickness.

Kelvin							
		Simulated		Experimental	Deviation	Error (%)	
		Yeoh	MR			Yeoh	MR
20 mm	**PLA (G)**	180.84	170.03	184.97	+3.47 −9.88	2.2	8.1
	TTP (ms)	6.00	5.00	5.42	+0.12 −0.06	10.6	7.8
		Simulated		**Experimental**	**Deviation**	**Error (%)**	
		Yeoh	MR			Yeoh	MR
30 mm	**PLA (G)**	110.28	122.82	120.72	+13.12 −5.15	8.6	1.7
	TTP (ms)	7.00	6.00	7.48	+0.09 −0.03	6.5	19.8
		Simulated		**Experimental**	**Deviation**	**Error (%)**	
		Yeoh	MR			Yeoh	MR
40 mm	**PLA (G)**	106.11	121.72	74.37	+3.71 −0.56	42.7	63.7
	TTP (ms)	8.00	7.00	8.67	+0.69 −0.06	7.7	19.2

Appendix A.2. PLA and TTP Data Results per Lattice Type and Thickness for FC Lattice

Table A2. FC lattice experimental and simulated impact results per thickness.

Face Centered Cubic							
		Simulated		Experimental	Deviation	Error (%)	
		Yeoh	MR			Yeoh	MR
20 mm	**PLA (G)**	240.71	182.63	265.95	+19.26 −1.95	9.5	31.3
	TTP (ms)	5.00	5.00	5.5	+0.09 0	8.8	8.8
		Simulated		**Experimental**	**Deviation**	**Error (%)**	
		Yeoh	MR			Yeoh	MR
30 mm	**PLA (G)**	127.20	123.77	105.68	+8.09 −0.43	20.4	17.1
	TTP (ms)	7.00	6.00	8.21	+0.09 −0.42	14.7	26.9
		Simulated		**Experimental**	**Deviation**	**Error (%)**	
		Yeoh	MR			Yeoh	MR
40 mm	**PLA (G)**	72.84	78.90	72.9	+5.99 −1.69	0.1	8.2
	TTP (ms)	10.00	9.00	10.09	+0.12 −0.12	0.9	10.8

Appendix A.3. PLA and TTP Data Results per Lattice Type and Thickness for BC Lattice

Table A3. BC lattice experimental and simulated impact results per thickness.

Body Centered Cubic							
		Simulated		Experimental	Deviation	Error (%)	
		Yeoh	MR			Yeoh	MR
20 mm	**PLA (G)**	239.61	165.92	250.26	+6.41 −6.15	4.3	33.7
	TTP (ms)	5.00	5.00	5.39	+0.21 −0.06	7.3	7.3
		Simulated		**Experimental**	**Deviation**	**Error (%)**	
		Yeoh	MR			Yeoh	MR
30 mm	**PLA (G)**	136.35	132.67	155.88	+6.16 −1.83	12.5	14.9
	TTP (ms)	7.00	6.00	7.36	+0.09 −0.12	4.9	18.5
		Simulated		**Experimental**	**Deviation**	**Error (%)**	
		Yeoh	MR			Yeoh	MR
40 mm	**PLA (G)**	81.072	106.25	149.31	+7.85 −1.44	45.7	28.8
	TTP (ms)	9.00	7.00	9.45	+0.48 −0.18	4.8	26.0

References

1. Baugh, C.M.; Kiernan, P.T.; Kroshus, E.; Daneshvar, D.H.; Montenigro, P.H.; McKee, A.C.; Stern, R.A. Frequency of Head-Impact–Related Outcomes by Position in NCAA Division I Collegiate Football Players. *J. Neurotrauma* **2015**, *32*, 314–326. [CrossRef] [PubMed]
2. Brown, S.; DeSimone, L.; Garlie, T.; Mitchell, B. Get Comfortable Being Uncomfortable: Variability in the Assessment of Perceived Comfort During Clothing and Individual Equipment Evaluations. Available online: https://journals.sagepub.com/doi/epdf/10.1177/1541931218621457 (accessed on 26 August 2026).
3. Nasim, M.; Spadoni, S.; Pavan, P.G.; Brasco, V.; Galvanetto, U. Helmets with Lattice Liners Can Mitigate Traumatic Brain Injury from Impacts. *J. Biomech.* **2024**, *176*, 112362. [CrossRef] [PubMed]
4. Sharma, R. TPU 3D Printing Powder Market Research Report 2034. Available online: https://marketintelo.com/report/tpu-3d-printing-powder-market (accessed on 26 August 2026).
5. Callister, W.D. Caractéristiques, Applications et Traitement Des Polymères. In *Science et Génie des Matériaux*; Dunod: Malakoff Cedex, France, 2001; pp. 418–454.
6. Yu, Z.; Savinov, R.; Matura, M.; Zhang, P.; Shi, J. Current Research Status on Advanced Lattice Structures for Impact and Energy Absorption Applications: A Systematic Review. *Thin-Walled Struct.* **2025**, *215*, 113490. [CrossRef]
7. Vaziri Sereshk, M.R.; Faierson, E.J. Concept Development for Innovative Functionally Graded Lattice Structures to Absorb Desired Energy and Impact. *Adv. Manuf.* **2025**, *13*, 799–812. [CrossRef]
8. Bolan, M.; Dean, M.; Bardelcik, A. The Energy Absorption Behavior of 3D-Printed Polymeric Octet-Truss Lattice Structures of Varying Strut Length and Radius. *Polymers* **2023**, *15*, 713. [CrossRef] [PubMed]
9. Chan, M.; Hung, S.; Yick, K.; Sun, Y.; Yip, J.; Ng, S. Impact Absorption Behaviour of 3D-Printed Lattice Structures for Sportswear Applications. *Polymers* **2025**, *17*, 2611. [CrossRef] [PubMed]
10. Wang, Y.; Xu, Z.; Wu, D.; Bai, J. Current Status and Prospects of Polymer Powder 3D Printing Technologies. *Materials* **2020**, *13*, 2406. [CrossRef] [PubMed]
11. Sun, J.S.; Lee, K.H.; Lee, H.P. Comparison of Implicit and Explicit Finite Element Methods for Dynamic Problems. *J. Mater. Process. Technol.* **2000**, *105*, 110–118. [CrossRef]
12. Hossain, M.; Steinmann, P. More Hyperelastic Models for Rubber-like Materials: Consistent Tangent Operators and Comparative Study. *J. Mech. Behav. Mater.* **2013**, *22*, 27–50. [CrossRef]
13. Qi, H.J.; Boyce, M.C. Stress–Strain Behavior of Thermoplastic Polyurethanes. *Mech. Mater.* **2005**, *37*, 817–839. [CrossRef]

14. Yang, G.; Wu, H.; Dong, H.; Huang, F. Compressive Behavior and Visco-Hyperelastic Constitutive of Polyurethane Elastomer over a Wide Range of Strain Rates. *Polym. Test.* **2024**, *138*, 108553. [CrossRef]
15. Mollaee, S.; Budgett, D.M.; Taberner, A.J.; Nielsen, P.M.F. Hyperelastic Constitutive Model Parameters Identification Using Optical-Based Techniques and Hybrid Optimisation. *Int. J. Mech. Mater. Des.* **2024**, *20*, 233–249. [CrossRef]
16. Sasso, M.; Palmieri, G.; Chiappini, G.; Amodio, D. Characterization of Hyperelastic Rubber-like Materials by Biaxial and Uniaxial Stretching Tests Based on Optical Methods. *Polym. Test.* **2008**, *27*, 995–1004. [CrossRef]
17. Mohotti, D.; Ali, M.; Ngo, T.; Lu, J.; Mendis, P. Strain Rate Dependent Constitutive Model for Predicting the Material Behaviour of Polyurea under High Strain Rate Tensile Loading. *Mater. Des.* **2014**, *53*, 830–837. [CrossRef]
18. Somarathna, H.M.C.C.; Raman, S.N.; Mohotti, D.; Mutalib, A.A.; Badri, K.H. Hyper-Viscoelastic Constitutive Models for Predicting the Material Behavior of Polyurethane under Varying Strain Rates and Uniaxial Tensile Loading. *Constr. Build. Mater.* **2020**, *236*, 117417. [CrossRef]
19. Oskui, A.E.; Cao, J.; Sadeghzade, S.; Yuan, H. Influence of Loading Mode on the Prediction Accuracy of Nonlinear Viscoelastic Models for Soft Adhesives. *Int. J. Solids Struct.* **2025**, *322*, 113595. [CrossRef]
20. Rifaie, M. Resilience and Toughness Behavior of 3D-Printed Polymer Lattice Structures: Testing and Modeling. Mater's Thesis, Wright State University, Dayton, OH, USA, 25 July 2017.
21. Shamim, R. Investigation of Bending and Crush Behaviors in Polymer Lattice Structures: Computational Approaches and Experimental Evaluation. *J. Reinf. Plast. Compos.* **2025**, *44*, 2981–2995. [CrossRef]
22. Nasim, M.; Hasan, M.J.; Galvanetto, U. Impact Behavior of Energy Absorbing Helmet Liners with PA12 Lattice Structures: A Computational Study. *Int. J. Mech. Sci.* **2022**, *233*, 107673. [CrossRef]
23. Martín-Sosa, E.; Távara, L.; Ojeda, J.; Estefani, A. Anisotropic and Hyperelastic Mechanical Response of 3D Printed TPU Parts. *Prog. Addit. Manuf.* **2025**, *10*, 5697–5709. [CrossRef]
24. Laird, G.; DuBois, P. *Impact Analysis of Polymeric Additive Manufactured Lattice Structures*; Predictive Engineering: Portland, OR, USA, 2024.
25. Diosdado-De la Peña, J.A.; Dwyer, C.M.; Krzeminski, D.; MacDonald, E.; Saldaña-Robles, A.; Cortes, P.; Choo, K. Low Impact Velocity Modeling of 3D Printed Spatially Graded Elastomeric Lattices. *Polymers* **2022**, *14*, 4780. [CrossRef] [PubMed]
26. Shepherd, T.; Winwood, K.; Venkatraman, P.; Alderson, A.; Allen, T. Validation of a Finite Element Modeling Process for Auxetic Structures under Impact. *Phys. Status Solidi B* **2020**, *257*, 1900197. [CrossRef]
27. Turnier Trottier, W.; Collin, A.; Krick, T.; Brailovski, V. LPBF-Produced Elastomeric Lattice Structures for Personal Protection Equipment: Mechanical Performance Versus Comfort-Related Attributes. *J. Manuf. Mater. Process.* **2025**, *9*, 182. [CrossRef]
28. EOS GmbH Flexible, Durable TPU for Automotive & Sports. Available online: https://www.eos.info/polymer-solutions/polymer-materials/data-sheets/mds-eos-tpu-1301 (accessed on 4 March 2026).
29. EOS GmbH. *EOS TPU 1301 Application Notes*; EOS GmbH: Krailling/Munich, Germany, 2020.
30. Ramirez, B.J.; Misra, U.; Gupta, V. Viscoelastic Foam-Filled Lattice for High Energy Absorption. *Mech. Mater.* **2018**, *127*, 39–47. [CrossRef]
31. Clauser, C.E.; McConville, J.T.; Young, J.W. *Weight, Volume, and Center of Mass of Segments of The Human Body*; Defense Technical Information Center: Fort Belvoir, VA, USA, 1969.
32. Ayedi, I.; Naifar, S.; Ramalingame, R.; Scholze, M.; Wagner, M.; Kanoun, O. Enhancing Electromechanical Performance of Extruded Piezoresistive Strain Sensors: Study of TPU Shore Hardness Effects. *J. Mater. Res. Technol.* **2025**, *37*, 3142–3154. [CrossRef]
33. Zulkifli, N.A.; Moon, G.D.; Hyun, D.C.; Lee, S. Comprehensive Constitutive Modeling and Analysis of Multi-Elastic Polydimethylsiloxane (PDMS) for Wearable Device Simulations. *Sci. Rep.* **2023**, *13*, 18413. [CrossRef] [PubMed]
34. Yeoh, O.H. Some Forms of the Strain Energy Function for Rubber. *Rubber Chem. Technol.* **1993**, *66*, 754–771. [CrossRef]
35. Welsim Mooney-Rivlin Hyperelastic Model for Nonlinear Finite Element Analysis. Available online: https://welsim.com/2021/05/24/mooney-rivlin-hyperelastic-model-for-nonlinear-finite-element-analysis.html (accessed on 8 May 2026).
36. Keerthiwansa, R.; Javořík, J.; Rusnáková, S.; Kledrowetz, J.; Gross, P. Hyperelastic Material Characterization: How the Change in Mooney-Rivlin Parameter Values Effect the Model Curve. *Mater. Sci. Forum* **2020**, *994*, 265–271. [CrossRef]
37. Holzapfel, G.A. *Nonlinear Solid Mechanics: A Continuum Approach for Engineering*; John Wiley & Sons: Chichester, UK, 2001; ISBN 0-471-82304-X.
38. Gomez-Jimenez, S.; Saucedo-Anaya, T.; Guerrero-Mendez, C.; Robles-Guerrero, A.; Silva-Acosta, L.; Navarro-Solis, D.; Lopez-Betancur, D.; Contreras Rodríguez, A.R. Mooney–Rivlin Parameter Determination Model as a Function of Temperature in Vulcanized Rubber Based on Molecular Dynamics Simulations. *Materials* **2024**, *17*, 3252. [CrossRef] [PubMed]
39. Rao, M.R.; Satayanarayana, M.R.S. On the Behaviour of Hyperelastic Materials, a Mooney-Riviln Approach. *Int. J. Eng. Res. Technol.* **2019**, *7*, IJERTCONV7IS03016.
40. Welsim Yeoh Hyperelastic Model for Nonlinear Finite Element Analysis. Available online: https://welsim.com/2021/05/25/yeoh-hyperelastic-model-for-nonlinear-finite-element-analysis.html (accessed on 8 May 2026).

41. Yahiaoui, M.; Denape, J.; Paris, J.-Y.; Ural, A.G.; Alcalá, N.; Martínez, F.J. Wear Dynamics of a TPU/Steel Contact under Reciprocal Sliding. *Wear* **2014**, *315*, 103–114. [CrossRef]
42. ANSYS Inc. 11.6. Hyperelasticity. Available online: https://ansyshelp.ansys.com/public/////Views/Secured/corp/v242/en/exd_ag/ds_non_linear.html (accessed on 16 July 2026).
43. Basloom, H.S. A Comparison Study between Tetrahedral Mesh and Hexahedral Mesh. In Proceedings of the 2018 21st Saudi Computer Society National Computer Conference (NCC), Riyadh, Saudi Arabia, 25–26 April 2018; pp. 1–6.
44. Katrojwar, A. Comparative Analysis of Hexahedral and Tetrahedral Mesh of Guide Bracket. *Int. J. Adv. Res. Ideas Innov. Technol.* **2021**, *7*, 490–492. [CrossRef]
45. Keerthiwansa, G.W.R.; Javořík, J.; Kledrowetz, J.; Nekoksa, P. Elastomer Testing: The Risk of Using Only Uniaxial Data for Fitting the Mooney-Rivlin Hyperelastic-Material Model. *Mater. Technol.* **2018**, *52*, 3–8. [CrossRef]
46. Bottlang, M.; DiGiacomo, G.; Tsai, S.; Madey, S. Effect of Helmet Design on Impact Performance of Industrial Safety Helmets. *Heliyon* **2022**, *8*, e09962. [CrossRef] [PubMed]
47. Emminger, C.; Çakmak, U.D.; Preuer, R.; Graz, I.; Major, Z. Hyperelastic Material Parameter Determination and Numerical Study of TPU and PDMS Dampers. *Materials* **2021**, *14*, 7639. [CrossRef] [PubMed]

Disclaimer/Publisher's Note: The statements, opinions and data contained in all publications are solely those of the individual author(s) and contributor(s) and not of MDPI and/or the editor(s). MDPI and/or the editor(s) disclaim responsibility for any injury to people or property resulting from any ideas, methods, instructions or products referred to in the content.